Validity of the unidirectional propagation model: application to laser-driven terahertz emission

J Déchard, A Nguyen, P González de Alaiza Martínez, I Thiele, Stefan Skupin, L Bergé

Validity of the unidirectional propagation model: application to laser-driven terahertz emission

Journal of Physics Communications

PAPER

Validity of the unidirectional propagation model: application to laser-driven terahertz emission

J Déchard[1], A Nguyen[1], P González de Alaiza Martínez[2], I Thiele[2], S Skupin[3] and L Bergé[1]

[1] CEA, DAM, DIF, F-91297, Arpajon, France
[2] Univ. Bordeaux—CNRS—CEA, Centre Lasers Intenses et Applications, UMR 5107, F-33405, Talence, France
[3] Institut Lumière Matière, UMR 5306 Université Lyon 1—CNRS, Université de Lyon, F-69622, Villeurbanne, France

E-mail: jeremy.dechard@cea.fr

Keywords: unidirectional pulse propagation equation, terahertz pulse generation, wave equation, Maxwell-fluid model

OPEN ACCESS

RECEIVED
28 July 2017

REVISED
5 September 2017

ACCEPTED FOR PUBLICATION
15 September 2017

PUBLISHED
13 December 2017

Abstract

The Unidirectional Pulse Propagation Equation (UPPE) is often used to compute the forward component of ultrashort light pulses in nonlinear materials. While its accuracy has frequently been reported for many applications in ultrafast optics, its validity can be questionable for ionizing pulses, in particular in the frequency domain below the electron plasma frequency ω_{pe}. Inaccuracy of the UPPE model in this frequency range may be detrimental to, e.g., a correct description of laser-driven terahertz emission. Here we demonstrate, analytically and numerically, that over long enough propagation paths, the one-dimensional solutions of both UPPE and the full wave equation match in the entire spectrum, including the spectral range $\omega \leqslant \omega_{pe}$. Our findings confirm the reliability of the UPPE solutions for a wide class of propagation problems.

1. Introduction

The propagation of a scalar electromagnetic field in $(1 + 1)$-dimensional geometry obeys the wave equation (WE) derived from Maxwell's equation [1]:

$$\partial_z^2 E - c^{-2}\partial_t^2 E = Q(E), \tag{1}$$

where $E(z, t)$ represents the electric field propagating along the z-axis, c is the speed of light in vacuum and $Q(E)$ is the response function that determines the linear and nonlinear properties of the material. In a centrosymmetric medium hosting free and bound electrons, this function decomposes as

$$Q(E) = \mu_0 \partial_t J + \mu_0 \partial_t^2 P, \tag{2}$$

which involves the plasma current density $J(z, t)$ and the macroscopic polarization $P(z, t)$. The latter quantity includes the nonlinear polarization, $P_{NL} = \epsilon_0 \chi^{(3)} E^3$, with $\chi^{(3)}$ representing the third-order susceptibility assumed to be instantaneous. ϵ_0 and μ_0 are the electric permittivity and the magnetic permeability in vacuum, respectively. For simplicity, we shall neglect linear gas dispersion in the forthcoming analysis. At moderate laser intensities and on short time scales, ion motion can be neglected. In the non-relativistic limit the electron current density reads as

$$\partial_t J + \nu_c J = \frac{e^2}{m_e} N_e E, \tag{3}$$

where ν_c, e, $N_e(z, t)$ and m_e are a phenomenological collision rate, and the electron charge, density and mass, respectively. In equation (3) the increase of free electrons is governed by the source equation

$$\partial_t N_e = W(|E|)(N_a - N_e), \tag{4}$$

where $W(|E|)$ is a field-dependent photoionization rate and N_a is the initial density of neutral atoms.

Generally, solving full Maxwell models accounting for multiple ionization processes as well as optical and plasma nonlinear effects is computationally expensive when simulating long propagation ranges as, e.g., in the

context of ultrashort pulse filamentation. Therefore, reduced models such as the Unidirectional Pulse Propagation Equation (UPPE) [2] are often preferred, assuming that the forward propagating component of the laser electric field conveys the major part of the energy and its coupling to the backward propagating component is negligible [3, 4]. The UPPE then describes the so-called 'forward' pulse component, propagating along positive longitudinal coordinates ($z > 0$). Expressed in $(1 + 1)$ dimensions, it governs the Fourier-transformed electric field $\tilde{E}(z, \omega)$ as

$$\partial_z \tilde{E}(z, \omega) - \mathrm{i}k\tilde{E}(z, \omega) = \frac{1}{2\mathrm{i}k}\tilde{Q}(z, \omega), \tag{5}$$

where tilde symbol refers to the Fourier transform:

$$\tilde{f}(z, \omega) = \int_{-\infty}^{+\infty} f(z, t)\mathrm{e}^{\mathrm{i}\omega t}\mathrm{d}t, \tag{6}$$

for an integrable function f and $k = \omega/c$. Equation (5) is used in ultrafast nonlinear optics to describe light pulses with ultrabroad spectra [5] and in higher dimensions it can describe pulse diffraction associated with transverse wave numbers $k_\perp$ through the formal change $k^2 \to k^2 - k_\perp^2$ [6].

The solution to the partial differential equation (1) is commonly advanced in time from a couple of initial/boundary conditions on E and its derivative. In contrast, equation (5) only requires the incident field value $E(z = 0, t)$ and it is solved along the longitudinal direction $z > 0$. Equation (5) may be refound from an easy factorization of equation (1), expressed in Fourier domain as [7–9]

$$(\partial_z - \mathrm{i}k)(\partial_z + \mathrm{i}k)\tilde{E} = \tilde{Q}. \tag{7}$$

Assuming weak enough nonlinearities, the field $\tilde{E}$ is decomposed as the sum of (quasi) linear forward (+) and backward (−) modes, $\tilde{E} = \tilde{E}_+\mathrm{e}^{\mathrm{i}kz} + \tilde{E}_-\mathrm{e}^{-\mathrm{i}kz}$. Substituting the previous quantities into equation (7), applying the approximation on the backward propagator: $(\partial_z + \mathrm{i}k)\tilde{E}_+\mathrm{e}^{\mathrm{i}kz} \approx 2\mathrm{i}k\tilde{E}_+\mathrm{e}^{\mathrm{i}kz}$, and conjecturing that both $\tilde{E}$ and $\tilde{Q}$ contain essentially the part corresponding to $\tilde{E}_+$ and $\tilde{Q}_+$, we then arrive to equation (5). In this simple derivation, the amplitude $\tilde{E}_+$ is supposed to be slow compared to $\mathrm{e}^{\mathrm{i}kz}$. This assumption is not necessary if more involved projection techniques are employed and if the PDE (1) is treated as an inhomogeneous second-order ODE [3, 4]. A pending issue about the solutions of equations (5) and (7) is thus their equivalence in the whole spectrum under the formal substitution $\partial_z + \mathrm{i}k \to 2\mathrm{i}k$. This equivalence is implicitly assumed *a priori* when one uses a UPPE model. Proving this statement *a posteriori*, by computing explicit solutions of these two models, remains to be done.

Over the past decade, the increasing potential of terahertz (THz) radiation has stimulated intensive efforts to develop efficient sources based on the ionization of gases by ultrashort laser pulses [10, 11]. In order to properly calibrate dedicated experiments, nonlinear propagation codes have to be particularly accurate in assessing the low-frequency part of the pulse spectrum. Different experiments and plasma conformations (e.g., micro-plasmas) have been recently examined, for which relevant THz emissions in frequency ranges below the electron plasma frequency were reported [12–14]. So far, however, the validity of the UPPE approach has received no numerical confirmation in this specific spectral range, which is often accessed in laser-driven THz experiments [15].

To highlight more this problematics, let us consider for a moment the elementary situation where the electron density is constant, as met in a preformed homogeneous plasma. Usually, solving equation (1) needs both initial and boundary conditions on $E(z, t)$, the evolution of which is monitored by the dielectric function that characterizes the medium's response to the electric field. In such a plasma with negligible collisions, the dielectric function expresses as $\epsilon(\omega) = 1 - \omega_{\mathrm{pe}}^2/\omega^2$, where $\omega_{\mathrm{pe}}^2 \equiv e^2 N_\mathrm{e}/(\epsilon_0 m_\mathrm{e})$ is the electron plasma frequency and ω is any Fourier frequency of the electromagnetic wave. When a monochromatic wave with frequency ω is incident on a vacuum-plasma boundary, only the fraction with real wave number $k_T = (\omega/c)(1 - \omega_{\mathrm{pe}}^2/\omega^2)^{1/2}$ is transmitted into the plasma [16]. Frequency components with $\omega \leqslant \omega_{\mathrm{pe}}$ are evanescent and vanish over the plasma skin depth. So, for Fourier components $\omega \leqslant \omega_{\mathrm{pe}}$, the incident pulse is mainly reflected and we expect this spectral range to damp out in the transmitted pulse along the propagation path, consistently. In contrast, for the UPPE model, plasma opacity is not present. This can be better appreciated when looking at the linear modes of the two equations for $N_\mathrm{e} = \text{const.}$, namely,

$$\tilde{E}(z, \omega) \sim \exp\left(\mathrm{i}k\sqrt{1 - \frac{\omega_{\mathrm{pe}}^2}{c^2k^2}}\, z\right) \tag{8}$$

for equation (1), and

$$\tilde{E}(z, \omega) \sim \exp\left[\mathrm{i}k\left(1 - \frac{\omega_{\mathrm{pe}}^2}{2c^2k^2}\right)z\right] \tag{9}$$

for equation (5). Obviously these two linear solutions do not match, in particular in the domain $\omega \leqslant \omega_{pe}$. The WE solution (8) vanishes exponentially as z exceeds about one plasma skin length $\delta_{pe} \equiv c/\omega_{pe}$ [17]. Accordingly, the UPPE solution (9) can in principle hold in the frequency range $\omega \gg \omega_{pe}$ only. In current applications, however, in which ω_{pe} varies through the time variations of the electron density $N_e(t)$, UPPE is supposed to be valid in the entire frequency range.

Whereas the solving for equation (1) can be performed exactly for a constant plasma frequency [16], the same problem becomes tricky when Q is a nonlinear function of E. This situation applies to a number of important issues in nonlinear optics and plasma physics [18, 19]. Here, we report that, surprisingly, both solutions to equations (1) and (5) become generically identical when the plasma is self-generated in time by the laser pulse. In this paper we indeed show that the THz pulse spectra and fields, when they are described either by a full *Maxwell-fluid* model—encompassing both backward and forward propagations—or by its UPPE approximation—modeling only the forward wave—match as the pulse propagates over distances larger than the plasma skin depth and its dynamics is mainly driven by the nonlinearities.

The paper is organized as follows: we derive in section 2 exact analytical solutions for the two WE and UPPE 1D models describing the secondary fields produced inside a collisionless plasma. In the framework of a perturbative approach, WE and UPPE solutions are shown to converge for long enough propagation distances. In section 3 we display numerical evidence by means of our 1D UPPE and MAXFLU codes that over distances $z > \delta_{pe}$, both WE forward and UPPE solutions indeed match in the THz spectral range and therefore provide similar THz fields. This statement is established for two-color femtosecond pulses and few-cycle single-color pulses as well, at intensities privileging Kerr or plasma responses. Section 4 concludes our investigation. Appendix describes the numerical implementation of the UPPE and MAXFLU codes.

2. The analytical solution

For technical convenience, we ignore collisional effects ($\nu_c \to 0$). Equations (1) and (5) have the plasma dispersion $\sim\omega_{pe}^2/\omega^2$ contained in the response function Q. The input laser profile at $z = 0$ is a two-color Gaussian pulse reading in time domain as

$$E_L(t, z = 0) = \sqrt{\frac{2I_0}{c\epsilon_0}}\left[\sqrt{1-r}\, e^{-2\ln 2\frac{t^2}{\tau_L^2}}\cos(\omega_0 t) + \sqrt{r}\, e^{-8\ln 2\frac{t^2}{\tau_L^2}}\cos(2\omega_0 t + \phi)\right], \tag{10}$$

where I_0 is the mean pump intensity, τ_L is the full-width-at-half-maximum (FWHM) duration of the fundamental pulse (the second harmonic has half pump duration), r denotes the relative intensity ratio of the second harmonic and ϕ is the relative phase between the two harmonics. One chooses a fundamental wavelength of $\lambda_0 = 1\ \mu$m related to the carrier wave frequency $\omega_0 \equiv 2\pi\nu_0 = 2\pi c/\lambda_0$, and an intensity ratio of $r = 0.1$ (two-color pulses) or 0 (single-color pulses). The interaction gas is argon at ambient pressure.The ionization rate $W(|E|)$ is given by the well-known quasi-static tunnel (QST) rate

$$W(|E(t)|) = \frac{\alpha}{|E(t)|}\exp\left[-\frac{\beta}{|E(t)|}\right], \tag{11}$$

where the constants α and β depend on the ionization potential of the gas [20, 21]. More complex rates describing multiple ionization events could be implemented as well [22]. These will be employed when investigating the highest intensity levels.

Because of the complex nonlinearities involved, we apply the same perturbation approach as in [23]. We decompose E into an unperturbed laser field, E_L, and an induced perturbation (secondary field), δE, namely, $E = E_L + \delta E$ with $\delta E \ll E_L$, so that the nonlinearity Q reduces to an inhomogeneous source term only evaluated on the laser field. Using equation (1) one obtains

$$(c^2\partial_z^2 - \partial_t^2)E_L = 0, \tag{12}$$

$$[(c\partial_z + \partial_t)(c\partial_z - \partial_t) - \omega_{pe}^2]\delta E = c^2 Q(E_L), \tag{13}$$

$$c^2 Q(E_L) = \omega_{pe}^2 E_L + \chi^{(3)}\partial_t^2 E_L^3. \tag{14}$$

Here, the perturbation δE contains the THz wave field, which can be extracted by means of a suitable frequency filtering. The electron plasma frequency ω_{pe} is a function of time through its dependency on $N_e(z,\ t)$. In the tunnel ionization regime, the electron density increases steplike and produces THz radiation by coupling with the high-frequency field $E_L(z - ct)$ [6]. In the framework of UPPE (equation (5)), the perturbation instead obeys

$$[-2\partial_t(c\partial_z + \partial_t) - \omega_{pe}^2]\delta E = c^2 Q(E_L). \tag{15}$$

Equations (13) and (15) must be solved with appropriate initial/boundary conditions. Looking for solutions propagating forward, it is natural to introduce the change of variables $\xi = z - ct, s = t$, transforming thereby

the WE and UPPE for the perturbation δE into

$$\text{WE}: \quad [\partial_s(2c\partial_\xi - \partial_s) - \omega_{\text{pe}}^2]\delta E = c^2 Q(E_{\text{L}}), \tag{16}$$

$$\text{UPPE}: \quad [\partial_s(2c\partial_\xi - 2\partial_s) - \omega_{\text{pe}}^2]\delta E = c^2 Q(E_{\text{L}}), \tag{17}$$

respectively. It is important to notice that E_{L} is only a function of ξ and thereby N_{e} and ω_{pe}^2, computed on the same laser field, only depend on ξ too. Our initial conditions for the WE read

$$\delta E(s,\, \xi = 0) = \delta E(s = 0,\, \xi) = 0, \tag{18}$$

yielding no constraint on the spatial derivatives. The pulse is sited in the half-plane $z < ct$ ($\xi < 0$ for causality reasons) and enters the plasma region at time $t = 0$. To satisfy the requirements (18), the input pulse ($z = 0$) is positioned in the plasma domain at $\xi_{\text{peak}} = -2\pi c\tau_{\text{L}}$ (see insets of figures 1(d) and (e)). Such boundary conditions offer flexibility to treat both UPPE and WE solutions in the same analytic framework. However, they differ from the inputs used in the numerical scheme of the UPPE1D and MAXFLU1D codes discussed in appendix. Therefore, we shall have to propagate over long enough distances $\geqslant c\tau_{\text{L}}/2$, ensuring the full development of the nonlinearities, in order to perform quantitative comparisons between the perturbed fields δE and their numerical counterparts. These boundary conditions also differ from those used in [23], where the progression of the laser pulse towards the plasma was described and the source term Q was tuned to zero for $z < 0$ in this reference.

For the WE, we now apply the Laplace transform $\widehat{f}\,(p) = \int_0^{+\infty} f\,(s)\mathrm{e}^{-ps}\mathrm{d}s$ onto equation (16) to get

$$[-p^2 + 2cp\partial_\xi - \omega_{\text{pe}}^2(\xi)]\widehat{\delta E} = \frac{c^2 Q(\xi)}{p}. \tag{19}$$

After some algebra we find straightforwardly

$$\delta E_{\text{WE}}(s,\, \xi) = \frac{c}{2}\int_0^{\xi} Q(\xi')\sqrt{\frac{2cs + \xi - \xi'}{G(\xi,\, \xi')}}\, J_1\left[\frac{\sqrt{G(\xi,\, \xi')}}{c}\sqrt{2cs + \xi - \xi'}\right]\mathrm{d}\xi', \tag{20}$$

where J_1 is the Bessel function of the first kind and

$$G(\xi,\, \xi') = \int_{\xi}^{\xi'} \omega_{\text{pe}}^2(u)\mathrm{d}u \tag{21}$$

is positive ($\xi < 0$ and $\xi' \geqslant \xi$). In the original frame variables, this solution expresses as

$$\delta E_{\text{WE}}(z,\, t) = \frac{c}{2}\int_0^{z-ct} Q(\xi')\sqrt{\frac{z + ct - \xi'}{\int_{z-ct}^{\xi'} \omega_{\text{pe}}^2(u)\mathrm{d}u}}\, J_1\left[\frac{1}{c}\sqrt{\int_{z-ct}^{\xi'} \omega_{\text{pe}}^2(u)\mathrm{d}u\,(z + ct - \xi')}\right]\mathrm{d}\xi', \tag{22}$$

and its spectrum is obtained after taking Fourier transform in time t.

Applying the same treatment to equation (17), we get

$$[-2p^2 + 2cp\partial_\xi - \omega_{\text{pe}}^2(\xi)]\widehat{\delta E} = \frac{c^2 Q(\xi)}{p}, \tag{23}$$

yielding

$$\delta E_{\text{UPPE}}(z,\, t) = \frac{c}{\sqrt{2}}\int_0^{z-ct} Q(\xi')\sqrt{\frac{z - \xi'}{\int_{z-ct}^{\xi'} \omega_{\text{pe}}^2(u)\mathrm{d}u}}\, J_1\left[\frac{\sqrt{2}}{c}\sqrt{\int_{z-ct}^{\xi'} \omega_{\text{pe}}^2(u)\mathrm{d}u\,(z - \xi')}\right]\mathrm{d}\xi'. \tag{24}$$

From a first glance, equations (22) and (24) only differ by their linear kernel

$$K_{\text{WE}}(\xi') = \frac{c}{2}\sqrt{\frac{z + ct - \xi'}{G(z - ct,\, \xi')}}\, J_1\left[\frac{1}{c}G^{1/2}(z - ct,\, \xi')\sqrt{z + ct - \xi'}\right], \tag{25}$$

$$K_{\text{UPPE}}(\xi') = \frac{c}{\sqrt{2}}\sqrt{\frac{z - \xi'}{G(z - ct,\, \xi')}}\, J_1\left[\frac{\sqrt{2}}{c}G^{1/2}(z - ct,\, \xi')\sqrt{z - \xi'}\right]. \tag{26}$$

As the UPPE/WE pulses advance in the $(z,\, t)$ plane, the integration variable ξ' can cover all values from 0 to $\xi'_{\text{min}} = 0 - ct_{\text{max}}$, t_{max} being fixed by the boundary of the time window ($t_{\text{max}} = 3.3$ ps here). Both UPPE and WE solutions converge towards each other at coordinates satisfying $z \gg |z - ct| > |\xi'|$, as this condition assures that $K_{\text{UPPE}}(\xi') \to K_{\text{WE}}(\xi')$. This requirement can indeed be understood from applying simple Taylor expansions in the argument $\sqrt{z + ct - \xi'} \approx \sqrt{2z}\sqrt{(z + ct)/(2z)}$ of the WE solution whenever $z \gg \xi'$, whereas $\sqrt{2}\sqrt{z - \xi'} \approx \sqrt{2z}$ in the UPPE solution in the same limit. These behaviors show that the UPPE solution is missing a dependency in the $(z + ct)$ propagation variable associated with a backward component. Applying

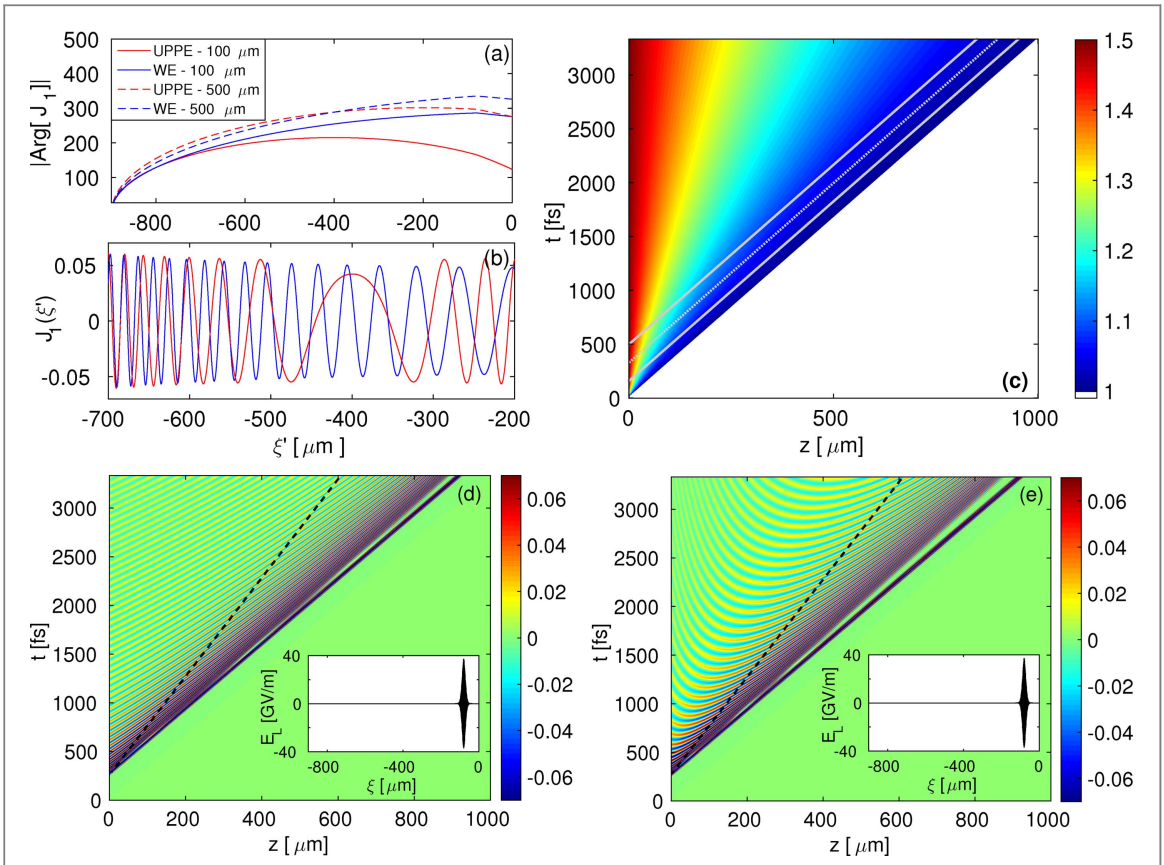

Figure 1. (a) Arguments of the Bessel function J_1 for the WE solution (22) (blue curves) and the UPPE solution (24) (red curves) for different distances z and at the upper bound $t = t_{max} = 3.3$ ps of the temporal window. $\omega_{pe}(t)$ increases in time according to the QST rate (11) for a two-color Gaussian pulse (1 μm + 0.5 μm) with 50 fs FWHM duration and 150 TW cm^{-2} peak intensity. (b) The function $J_1(X)$ for the WE solution (blue curves) and the UPPE solution (red curves) at $z = 100$ μm. The plasma frequency is reached at $\xi' \approx -600$ μm. (c) (z, t) map of the ratio $\delta E_{WE}/\delta E_{UPPE}$ as defined by equation (27) with constant source term Q. The grey dotted line identifies the location of the laser peak at $\xi = \xi_{peak}$ and the grey solid lines delimit the domain of the laser pulse. (d and e) (z, t) maps of the full analytical solutions (d) equation (22) and (e) equation (24) with a non-constant source term driven by the same two-color 50 fs pulse. Insets show the input pulse in the plasma domain $\xi < 0$. The black dashed lines delimit the convergence domain of the UPPE and WE solutions, which increases with the coordinate z.

the second inequality $z \gg |z - ct|$ in the previous approximations leads to the convergence of the two solutions.

This property is reflected by figure 1(a), which plots the argument of the Bessel function for a two-color 50 fs Gaussian pump pulse with 150 TW cm^{-2} intensity. Here, the pulse region extends over $|\xi'| < 100$ μm and we can observe the convergence of the two Bessel arguments when the distance z is increased from 100 to 500 μm. Concerning their potential discrepancies, one can observe that, at large times ($|\xi'| > 100$ μm), the plasma frequency ω_{pe} is constant, so that $G(z - ct, \xi') = \omega_{pe}^2(\xi' - z + ct)$. The oscillations in the WE/UPPE solutions are then dictated by those of the Bessel function J_1. At times corresponding to $\xi' \approx -600$ μm and $z = 100$ μm, these oscillations relax on the plasma period as $J_1(X_{WE}) \sim t^{-1/2}\sin(\omega_{pe}t/c)$ in the WE solution. In contrast, $J_1(X_{UPPE})$ relaxes to the function $\sim t^{-1/2}\sin(\omega_{pe}\sqrt{2t/c})$, which develops slower oscillations around the maximum values of the Bessel arguments. Figure 1(b) thus displays evidence of a minimum frequency smaller than ω_{pe} in the UPPE solution, whose value increases with z until reaching the electron plasma frequency.

To get more insight into the convergence dynamics, we may also consider a much simpler situation by assuming a constant inhomogeneity Q. With the help of equations (22) and (24), this yields the ratio

$$\frac{\delta E_{WE}}{\delta E_{UPPE}} = 1 - \frac{1}{2}\left(\frac{z - ct}{z + ct}\right), \tag{27}$$

which can be useful to understand the differences induced by the linear propagators. Figure 1(c) shows equation (27) as a function of z and t. The lower-right part ($z > ct$), in which our solutions are not defined, is set to zero for causality reason. Both WE and UPPE solutions converge as long as $z \gg |z - ct|$, which includes the laser region. In contrast, the same solutions depart from each other in the sharper limit $ct \gg z$. Let us now imagine that, in the vicinity of the pulse head, the source term Q has a certain finite extent, schematically delimited by the two grey solid lines in figure 1(c). The WE and UPPE solutions converge near the laser head, where they are dominated by the nonlinearities computed on the laser profile. In the opposite domain, the

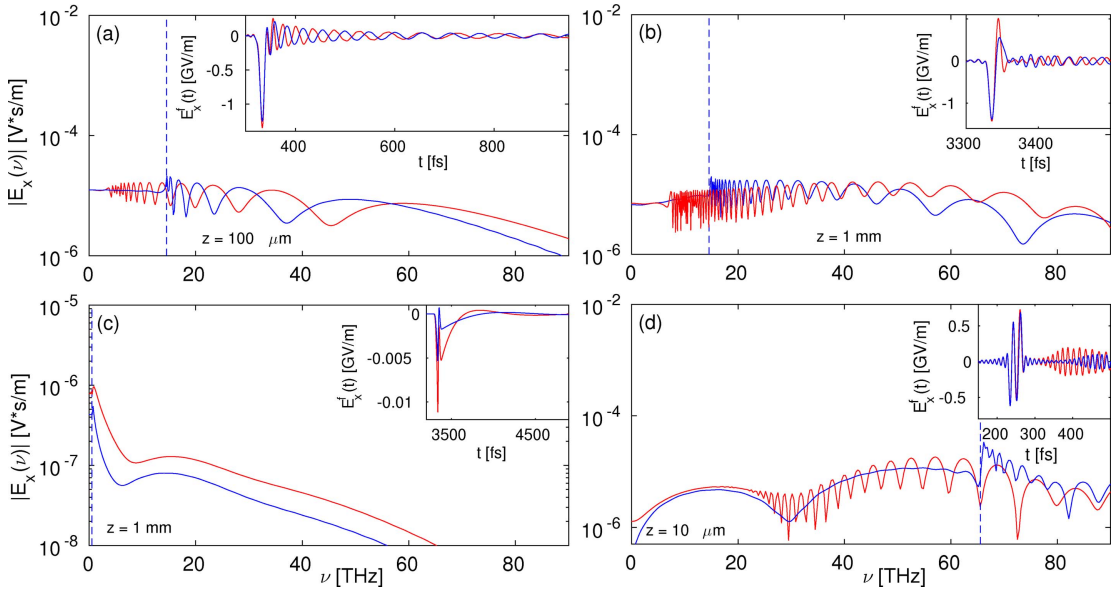

Figure 2. Spectra at (a) $z = 100$ μm and (b) $z = 1$ mm plotted from the analytical solutions (22) (WE, blue curves) and (24) (UPPE, red curves) for a two-color Gaussian pulse with mean pump intensity of 150 TW cm^{-2} and FWHM duration of 50 fs interacting with argon. Note the oscillations in the UPPE spectrum for $\nu \leqslant \nu_{pe}$ and the growth in ν_{min} as z increases. Same quantities at (c) $z = 1$ mm for $I_0 = 50$ TW cm^{-2} and (d) $z = 10$ μm for $I_0 = 1$ PW cm^{-2}. The vertical dashed lines indicate the plasma frequency.

solutions are mainly driven by their linear propagators that behave differently over large times. However, the larger the propagated distance z, the broader the convergence domain, which spans a cone in the $(z,\ t)$ plane (see blue area in figure 1(c)). This is confirmed by figures 1(d) and (e) that detail the field amplitudes in the $(z,\ t)$ plane computed from the complete expressions (22) and (24). One can see that the UPPE field contours differ from the WE contours in the spatio-temporal domain $ct \gg z$. In particular, a hyperbolic distribution occurs, associated with the longer periods of figure 1(b) and with the fact that UPPE does not admit pulse components varying with $z + ct$. Nevertheless, the solutions achieve the same dominant component near the nonlinearity region, where they mutually converge and whose area grows with z (see figures 1(d) and (e) where convergence is reached inside the cones delimited by black dashed lines).

Figures 2(a) and (b) show some examples of analytical UPPE/WE spectra and fields for a two-color Gaussian pulse with FWHM duration of 50 fs, 150 TW cm^{-2} overall intensity. The nonlinearities consist of plasma generation alone. Here and in the following the THz fields shown as insets are computed from an inverse Fourier transform of $\delta\tilde{E}$ in the frequency window $\nu \equiv \omega/2\pi \leqslant 90$ THz. The plotted propagation distances are $z = 100$ μm and $z = 1$ mm. One can observe that (i) the spectral region $\nu < \nu_{pe} \equiv \omega_{pe}/2\pi$ becomes depleted as z increases, (ii) the minimum frequency marking the UPPE spectrum, ν_{min}, increases in turn, and (iii) in the rear part of the pulse (beyond the laser head) the UPPE linear mode consistently develops longer periods (see inset of figure 2(a)).

At smaller intensity ($I_0 = 50$ TW cm^{-2}) and with zero phase angle ($\phi = 0$), the Kerr response is expected to be a key player [24]; so we now include it. A typical Kerr-plasma spectrum at weak intensity is illustrated in figure 2(c), where the low plasma frequency, $\nu_{pe} = 0.53$ THz, highlights the lesser contribution of photoionization and a parabolic spectral shape characterizes the Kerr signature in the band of higher THz frequencies ($\nu \approx 10 - 20$ THz) [11]. For a mean pump intensity $I_0 = 1$ PW cm^{-2}, in contrast, several electrons can be extracted from their atom. In this high intensity regime, the ionization of the successive electron shells of argon is described by the multiple-ionization model built in [22] and based on a field-dependent cycle-averaged rate computed from the Perelomov–Popov–Terent'ev (PPT) theory [25]. At short propagation distances, unlike the WE solution, the UPPE spectrum is not peaked at the plasma frequency $\nu_{pe} \approx 55$ THz, but it develops spectral oscillations in the region $\nu < \nu_{pe}$, as expected (figure 2(d)). At larger distances, discrepancies are amplified (not shown), because δE starts to break the underlying hypothesis of our perturbative approach, $\delta E \ll E_L$, as the perturbation itself produces optical frequencies ($\omega_0,\ 2\omega_0,\ ...$) through the nonlinearities, e.g., the photoionization. Since the optical pump pulse is not depleted along propagation, our formalism cannot assure a proper conservation of the electromagnetic energy. As a validity criterion we consider that our analytical solution stops to hold whenever the spectral intensity of δE at optical frequencies becomes comparable to $\sim$75% of the laser spectral intensity. Such limitations are of course absent in the results of the full numerical simulations, as can be inferred from, e.g., figure 6.

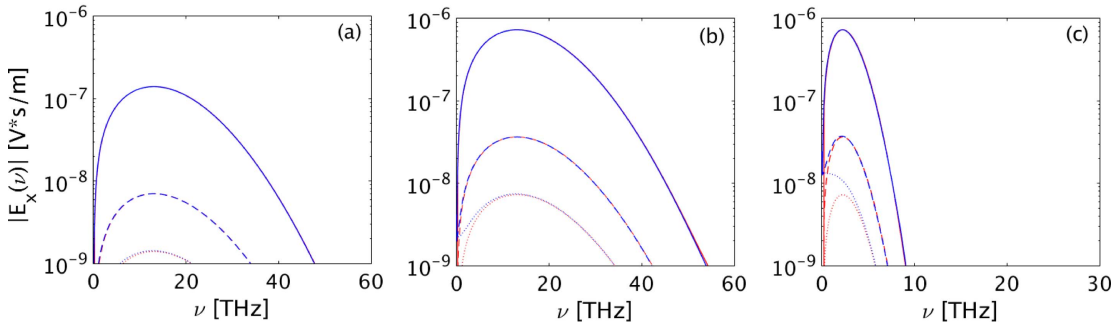

Figure 3. THz spectra at $z = 10$ μm (dotted curves), $z = 50$ μm (dashed curves) and $z = 1$ mm (solid curves) from the UPPE1D code (red curves) and the MAXFLU1D code (blue curves) for the intensities (a) 50 TW cm^{-2} and (b) 150 TW cm^{-2}, using a two-color 50 fs Gaussian pulse with zero phase difference. (c) Same for a 300 fs two-color Gaussian pulse with 150 TW cm^{-2} intensity. Only the Kerr effect is taken into account.

3. Numerical results

Our theoretical expectations are tested by running the MAXFLU1D and UPPE1D codes, whose respective numerical schemes are detailed in appendix. For both codes the input condition at $z = 0$ is the two-color Gaussian pulse defined above by equation (10). The pump intensity is alternatively set to 50, 150 and 1000 TW cm^{-2} in order to investigate various ionization degrees. The phase angle ϕ is valued as $\phi = 0$ to enhance the Kerr effect in the 50 TW cm^{-2} case and $\pi/2$ otherwise [24]. For Gaussian pulses with moderate laser intensity, from 50 to 150 TW cm^{-2}, and undergoing single ionization, we employ the QST rate (11). Consistently with section 2, when dealing with 1 PW cm^{-2} pulses, multiple ionization will be described from the multi-ion model of [22] employing the field-dependent PPT ionization rate.

To start with, only the Kerr response is accounted for [$n_2 = 3\chi^{(3)}/4\epsilon_0 c = 1 \times 10^{-19}$ cm^2 W^{-1}] and we first ignore plasma generation ($N_e = 0$) and collisions. Figures 3(a) and (b) show the spectra of the THz fields produced in argon by a 50 fs two-color pulse with 1 μm fundamental pump wavelength at increasing propagation distances, when using the UPPE and the MAXFLU codes. Although the WE and UPPE spectra may not perfectly match over the shortest propagation distances, e.g., $z = 10$ μm, an excellent agreement is found at further distances $z \geqslant 50$ μm for both intensities. These simulations show that, in the absence of plasma generation, both WE and UPPE solutions match in the whole spectral domain over relatively short distances $\approx$10 μm. This property is independent of the pulse duration, which has been counterchecked by another simulation using longer pump duration, $\tau_L = 300$ fs (see figure 3(c)). Here, the two UPPE and MAXFLU spectra match again over distances less than the pulse length $\sim$90 μm. Minor early discrepancies are linked to small differences in the initialization of the numerical codes. The convergence speed between the WE and UPPE spectra driven by a Kerr response alone thus does not depend on the distance propagated over the pulse length $c\tau_L$. This behavior is rather logical, as the Kerr nonlinearity is just treated as a perturbation in the source term Q and does not impact the frequency range of the linear modes in equations (8) and (9).

Next, in figure 4, only plasma generation is taken into account, similarly to figures 2(a) and (b). So, the Kerr response and collisions are set equal to zero. The selected intensity level is $I_0 = 150$ TW cm^{-2}. When the backward-propagation operator is dropped out, the fundamental linear modes beating at the electron plasma frequency ω_{pe} are lost and no plasma opacity is allowed, which results in the development of oscillatory components in the frequency range $\nu < \nu_{pe}$ of the UPPE spectrum. This is consistent with the linear mode of equation (9) that admits non-zero frequency components in the range $\omega_{pe}/\sqrt{2} \leqslant \omega \leqslant \omega_{pe}$. In contrast, the MAXFLU spectrum is dominated by plasma current oscillations, which prevail as long as the propagation distances remain of a few plasma skin depths (here, $\delta_{pe} = 3.3$ μm), as evidenced by figure 4(b). Over longer distances, however, both UPPE and MAXFLU spectra merge in the range $\nu > \nu_{pe}$, as photocurrents become the dominating source in the THz generation process. Out off the laser head, long oscillations over longer times proceed from the Bessel function discussed above. Besides the good agreement between our analytical solutions shown in figures 2(a) and (b) and the numerical solutions of figures 4(c) and (d), we can observe that:

- At large times the field oscillations are slower for the UPPE solution than for the WE solution (see insets). The oscillation frequency increases as the optical path is augmented.

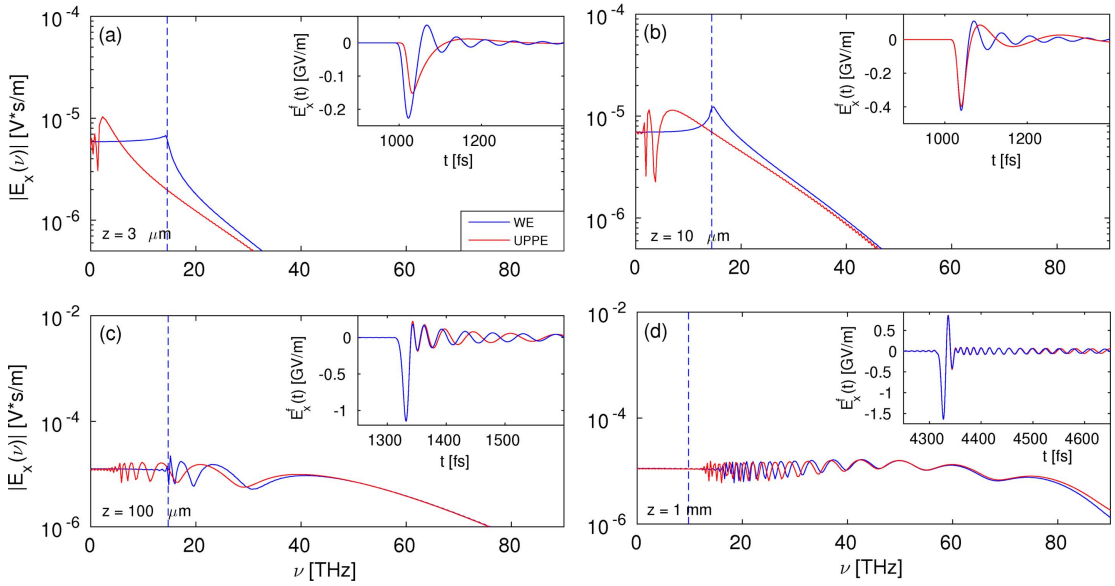

Figure 4. THz spectra and fields (see insets) at different propagation distances computed from the UPPE1D code (red curves) and the MAXFLU1D code (blue curves) for a two-color 50 fs Gaussian pulse with 150 TW cm^{-2} intensity: (a) $z = 3$ μm (corresponding to almost one plasma skin depth δ_{pe}), (b) $z = 10$ μm, (c) $z = 100$ μm, and (d) $z = 1$ mm. Vertical dashed lines indicate $\nu = \nu_{pe}$.

- Whereas, as expected, the spectral region $\nu < \nu_{pe}$ is flat in the forward WE solution from $z = 3$ μm, the UPPE spectrum develops oscillations from a minimum frequency ν_{min} that increases with the propagation distance z.
- Convergence is almost reached at $z = 1$ mm. The equality $\nu_{min} = \nu_{pe}$ (associated to the plasma response of the input field) is met at $z = 1$ cm and spectra match for all frequencies (not shown).

For comparison, figures 5(a) and (b) show the same quantities when including the Kerr response of argon and electron-neutral collisions with the averaged rate $\nu_c = 1/190$ fs$^{-1} = 5.3$ ps^{-1}. At 150 TW cm^{-2} intensity, one reports a comparable matching rate between the two spectra and fields, being even sped up by the damping of oscillations at low frequencies <10 THz and the decrease of the current density in time. Indeed the collision term damps the free electron current in equation (3) and thus both UPPE and MAXFLU solutions are also damped to zero over long times ($\gg$190 fs) beyond the laser head. The green curve shows the backward spectrum collected at $z = -10$ μm from the vacuum-plasma interface in the MAXFLU simulation. This spectrum occupies the region $\nu \leqslant \nu_{pe}$, as expected [5, 23], since it is emitted by plasma current oscillations over the plasma skin depth. This backward spectrum remains unchanged over propagation in vacuum.

Similar properties of matching can be refound between the solutions of the two models for pulse configurations favoring either a weaker plasma response (thus a more efficient Kerr effect) at smaller intensities or a stronger plasma response achieved at higher intensities. Figures 5(c) and (d) display the evolution of the same two-color pulse having an input intensity of 50 TW cm^{-2}. The pulse is undergoing an effective Kerr response combined with plasma generation in argon. The corresponding plasma frequency is very weak, $\nu_{pe} = 0.53$ THz, which is related to a long plasma skin depth $\delta_{pe} \simeq 90$ μm. Even at rather weak spectral amplitudes, the WE and UPPE spectra and fields approach to each other over distances exceeding far this depth, at least from 1 mm, which confirms the important role of the plasma skin depth in the matching process. The spectral shape follows its analytical counterpart plotted in figure 2(c) for $z = 1$ mm. The numerical UPPE/WE spectra merge from $z = 5$ mm until perfectly overlapping at $z = 1$ cm (figure 5(d)).

In the opposite range of pulse intensities, $I_0 = 1$ PW cm^{-2}, the peak plasma density increases and a much shorter plasma skin depth—$\delta_{pe} \approx 0.75$ μm for $\nu_{pe} \approx 65$ THz as imposed by the incident pulse—should lead to a quicker merging between the UPPE and WE solutions. Matching is indeed achieved at about $z = 50$ μm, i.e., over a few tens of δ_{pe} (see figures 6(a) and (b)). The optical field distortions induced by self-steepening and plasma generation are plotted as inset in figure 6(b). They also show a good agreement between the WE and UPPE models at distances >10 μm. The spectral distributions and THz field amplitudes (inset of figure 6(a)) still reasonably agree with those computed at $z = 10$ μm from our analytical solution (figure 2(d)). Besides, for the same high intensity level, it has been recently shown that photocurrents could be the main player for single-color

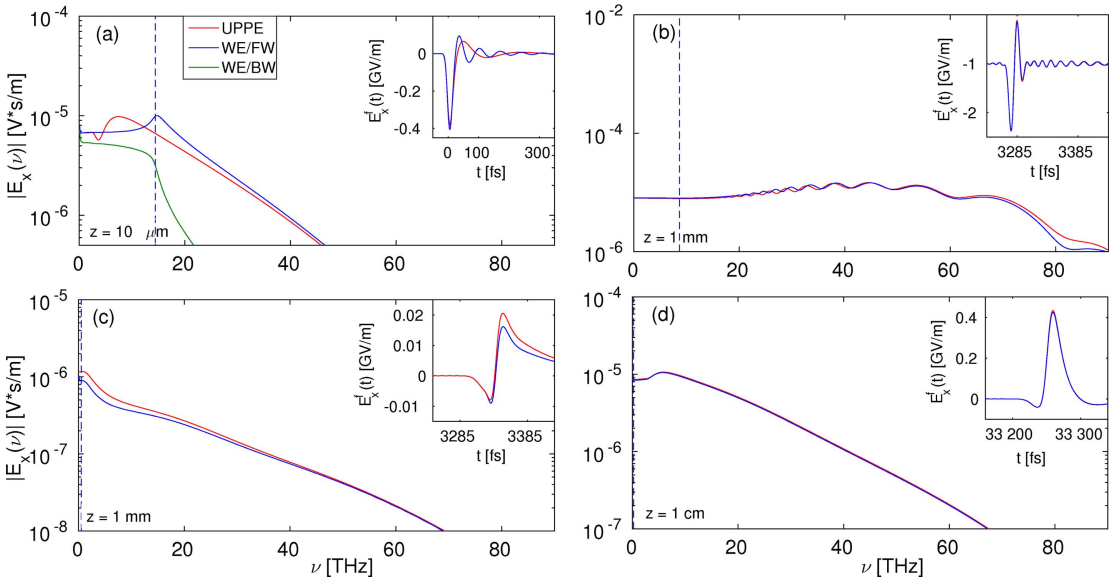

Figure 5. Same as in figure 4 with same color plotstyle but with the Kerr term and electron-neutral collisions included for $I_0 = 150$ TW cm^{-2} at (a) $z = 10$ μm, (b) $z = 1$ mm and $I_0 = 50$ TW cm^{-2} at (c) $z = 1$ mm, (d) $z = 1$ cm. In (a) the green curve plots the backward spectrum collected at $z = -10$ μm.

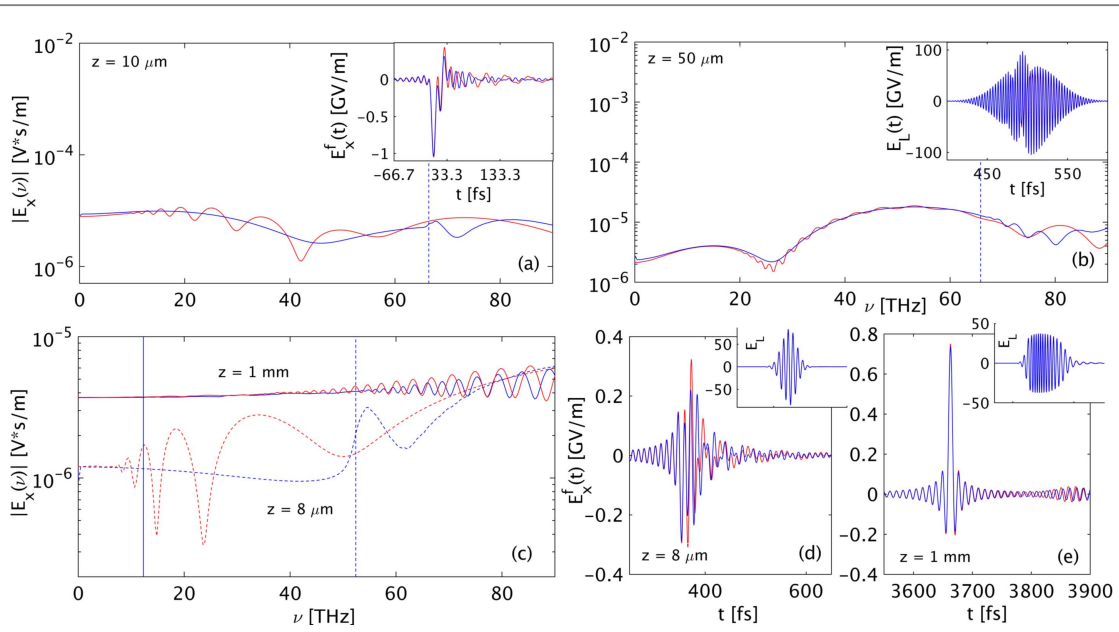

Figure 6. THz spectra with 1 PW cm^{-2} laser intensity at (a) $z = 10$ μm and (b) $z = 50$ μm for a two-color 50 fs Gaussian pulse computed from the UPPE (red curves) and MAXFLU codes (blue curves). Insets show the THz field at $z = 10$ μm and the overall laser field at $z = 50$ μm. (c–e) THz spectra and fields for a single-color (1 μm) Gaussian pulse with 8 fs FWHM duration interacting with Ar at 1 PW cm^{-2} intensity. (c) THz spectra at $z = 8$ μm (dashed curves) and $z = 1$ mm (solid curves). (d, e) Corresponding THz fields. Laser field patterns are shown as inset. Vertical lines point out to $\nu = \nu_{pe}$ (with corresponding plotstyles in (c)).

pulses, provided that the pulse duration be short enough, i.e., few-cycle [13]. For this purpose, figures 6(c)–(e) show two spectra computed from a 1 μm Gaussian pump pulse with 8 fs FWHM duration at 1 PW cm^{-2} intensity and evolving from $z = 8$ μm ($\delta_{pe} \approx 1$ μm). Again the UPPE and WE spectra nicely approach to each other in the range $\nu > \nu_{pe}$ from $z \approx 100$ μm (not shown) and they overlap in the whole spectral range at $z \approx 1$ mm.

In order to illustrate the influence of the electron dynamics that can vary through laser distortions, figures 7(a) and (b) finally show the electron density corresponding to figures 5(a), (b) and 6(c). Between the

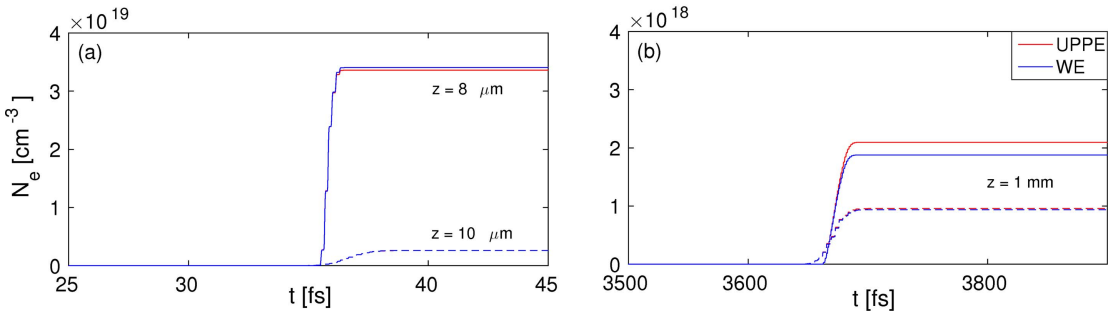

Figure 7. Electron density computed from the UPPE1D code (red curves) and the MAXFLU1D code (blue curves) for an 8 fs pulse with 1 PW cm^{-2} peak intensity (solid lines, single color), and a 50 fs pulse with 150 TW cm^{-2} peak intensity (dashed lines, two colors) at (a) $z = 8$ μm and $z = 10$ μm, and (b) $z = 1$ mm.

two plotted distances, one reports for the 8 fs pulse with 1 PW cm^{-2} peak intensity a decrease by half the maximum field value resulting in one decade decrease in the electron density. For comparison, the 50 fs pulse with 150 TW cm^{-2} peak intensity keeps comparable density levels. The matching distance of the UPPE/WE solutions for those two configurations then become similar: at $z = 1$ mm, the 8 fs pulse with 1 PW cm^{-2} peak intensity has almost the same charge level as the 50 fs pulse with 150 TW cm^{-2} peak intensity, and has thus a comparable plasma skin length ($\delta_{\rm pe} = 3.8$ versus 5.4 μm) at this distance. The two skin depths only differ from each other by a factor $\sim\sqrt{2}$ and, therefore, the two fields display comparable convergence speed between the two models. This justifies that the number of skin depths needed for matching the two solutions is not universal, as it also depends on the changes in the electron density induced by the distortions of the laser field along propagation. Similar behaviors could be reported from longer (300 fs) pulses (not shown).

4. Conclusion

In summary, we have derived one-dimensional analytical solutions describing both bidirectional (WE) and unidirectional (UPPE) propagating light pulses by means of a perturbative approach. Structural differences between the WE and UPPE solutions have been explored thanks to those analytical solutions, especially the shape of the THz spectra over mm-range propagation distances. The convergence between both solutions in the $(z,\ t)$ plane has been examined from direct numerical computations integrating Maxwell-fluid equations and the unidirectional pulse propagation model. Even if discrepancies in the linear propagators occur at large times beyond the laser head ($ct \gg z$), the UPPE solution matches its WE counterpart in the $(z,\ t)$ region where the nonlinearity is effective. The extent of the convergence region increases with the propagation distance. Numerical simulations covering a wide range of pulse configurations confirm that, over a propagated distance larger than some plasma skin depths, the UPPE and Maxwell-fluid solutions superimpose to one another. As a result, WE and UPPE spectra match remarkably well over all the spectrum, including the range $\omega \leqslant \omega_{\rm pe}$.

To conclude, we demonstrated that, in a one-dimensional geometry, the UPPE model, which only governs the forward pulse component, is able to provide similar spectra to a bidirectional Maxwell-fluid model over distances where Kerr nonlinearities as well as photocurrents drive THz pulse generation. Further studies should aim at testing this property in full 3D propagation geometries.

Acknowledgments

JD and LB thank Arnaud Debayle for fruitful discussions on the analytical solutions. This work was supported by the ANR/ASTRID Project 'ALTESSE' # ANR-15-ASTR-0009 and performed using HPC resources from GENCI (Grant # A0010506129 and # A0020507594). SS acknowledges support by the Qatar National Research Fund through the National Priorities Research Program (Grant # NPRP 8-246-1-060).

Appendix. The 1D UPPE and MAXFLU codes

The UPPE1D code solves equation (5) coupled with the fluid equations (3) and (4) propagating over the optical axis z. A second-order accurate split-step scheme allows us to separate the linear and the nonlinear parts of the

UPPE equation [26]. The linear part (propagation) is solved exactly in the Fourier space as follows:

$$\tilde{E}(z + \Delta z, \omega) = \tilde{E}(z, \omega)\exp[ik(\omega)\Delta z], \tag{A.1}$$

where $k(\omega) = \omega/c$. Then, the nonlinear contribution, including the Kerr terms, ionization and absorption losses, are advanced over one spatial step Δz according to the equation

$$\left[\partial_z E(t) + \partial_t\left(\frac{\chi^{(3)}}{2c}E(t)^3\right)\right] = -\mathcal{F}^{-1}\left[\frac{c\mu_0}{2}(\tilde{J}(\omega) + \tilde{J}_{\rm loss}(\omega))\right], \tag{A.2}$$

where $\mathcal{F}^{-1}$ means inverse Fourier transform, $J_{\rm loss}$ refers to a loss current due to photoionization, usually negligible in laser–gas interactions. The left-hand side of equation (A.2), which accounts for Kerr polarization, is first discretized in time by finite volumes at time step j ($t = j\Delta t$) as

$$\partial_z E_j = -\frac{1}{\Delta t}[\Phi_{j+1/2} - \Phi_{j-1/2}], \tag{A.3}$$

where $\Phi_{j+1/2}$ refers to the numerical flux between two neighboring cells, j and $j + 1$, of the grid. Following the well-known Godunov's method [27], the numerical flux is given here by

$$\Phi_{j+1/2} = \frac{\chi^{(3)}}{2c}E^3_{j+1/2}, \tag{A.4}$$

where $E_{j+1/2}$ accounts for the solution to the Riemann problem at the intercell $j + 1/2$ [28], which aims at solving the advected solution constrained by two constant states indexed by j and $j + 1$ on both sides of the intercell. In this case, the solution to the Riemann problem is straightforward: with $\chi^{(3)} \geqslant 0$, at first-order of accuracy, one has to take simply $E_{j+1/2} = E_j$. To achieve second-order accuracy, we do a linear reconstruction of $\{E_j\}$ following the Essentially Non-Oscillatory technique [28]:

$$E_{j+1/2} = E_j + \frac{\Delta_j}{2}, \tag{A.5}$$

where Δ_j compares the downwind difference $(E_{j+1} - E_j)$ and the upwind difference $(E_j - E_{j-1})$ and retains the lower value in modulus. Limiting the slope in this way allows us to avoid Gibbs oscillations when optical shocks induced by self-steepening occur [29]. With the second-order numerical flux, we can rewrite equation (A.2) as:

$$\partial_z E_j = -\frac{1}{\Delta t}[\Phi_{j+1/2} - \Phi_{j-1/2}] - F^{-1}\left[\frac{c\mu_0}{2}(\tilde{J}(\omega) + \tilde{J}_{\rm loss}(\omega))\right]_j, \tag{A.6}$$

which is easily solved by the second-order Runge–Kutta method. Using this discretization, provided that $\chi^{(3)}$ is weak enough, the maximum spatial step given by the Courant–Friedrichs–Lewy (CFL) stability condition of equation (A.3) is $\Delta z_{\rm max} = 2c\Delta t/(3\chi^{(3)}E_0^2)$, with E_0 denoting the input amplitude of the laser field. This step is much larger than the spatial steps needed to obtain accurate solutions of equation (A.2) as well as those requested to integrate the WE model. Long propagation distances can then be simulated in reasonable amount of computational time with the UPPE approach.

The *Maxwell-fluid* code, named MAXFLU1D, is based on a finite volume scheme solving the WE (1) and fluid equations (3) and (4) in time. This set of equations is re-expressed in the conventional conservative form of a nonlinear hyperbolic system, e.g., for the transverse (x-polarized) field $E \equiv E_x$ through the electric displacement D_x:

$$\partial_t D_x + \mu_0^{-1}\partial_z B_y = -(J_x + J_{x,\rm loss}), \tag{A.7}$$

$$\epsilon_0^{-1}D_x = E_x + \chi^{(3)}E_x^3. \tag{A.8}$$

This nonlinear hyperbolic system is treated numerically by splitting the advection part (source terms set equal to zero) and the evolution part (source terms included but with zero derivative in z) at every time step Δt along an evolution-advection-evolution algorithm. First, the evolution stage is solved by using a second-order Runge–Kutta scheme. Next, the Maxwell and Fluid advective parts, which are independent of each other, are solved over Δt. For the former advection, the Lax–Wendroff scheme is chosen (second-order accurate) [30], even though some Gibbs oscillations might appear. For the latter advection stage, instead, we couple a First Order Centered scheme [28], which is first-order accurate, to the Lax–Wendroff scheme, following the Flux Corrected Transport approach [31]. This is necessary for treating the fluid advection; otherwise strong Gibbs oscillations may occur in the neighborhood of electron density gradients, which can render the code unstable. The calculation domain is a sliding window that moves forward at the speed of light c and, even when accounting for the Kerr-induced changes in the optical refractive index, the CFL condition of the (t, z) grid, $\Delta z = c\Delta t$, is the standard requirement.

In the UPPE1D code, the THz field driven by the laser field is 0 at $z = 0$. One spatial step further, the laser pulse enters the medium and triggers nonlinearities, producing thus a non zero THz field. In the MAXFLU1D code, the THz field grows from a laser pulse crossing a vacuum-plasma interface and admits backward

contributions. Since we are interested in THz generation, one should use simultaneously a fine spectral resolution and a fine time step in order to correctly describe the low frequency spectrum below ν_{pe} and the two-color laser pulse components including its higher harmonics generated along propagation. The time window of our simulations is, therefore, set to 3.33 ps corresponding to a frequency step of $\Delta\nu = 0.3$ THz. The time step Δt is tuned from $\lambda_0/(128c)$ down to $\lambda_0/(512c)$ leading to a spatial step of $\Delta z = \lambda_0/128$ resp. $\Delta z = \lambda_0/512$ for the MAXFLU simulations (CFL condition) and it is fixed to $\Delta z = \lambda_0/25$ for the UPPE simulations. The highest resolutions used in the MAXFLU code have been employed when it was necessary to decrease the background noise in the lowest parts of the pulse spectrum (e.g., for a Kerr response alone).

Let us finally notice that, so far, we have neglected linear dispersion $P_L = \epsilon_0 \chi^{(1)} * E$, with $\chi^{(1)}$ representing the first-order susceptibility and $*$ standing for the convolution product in time. Linear gas dispersion can be accounted for as well through the pulse wave number $k(\omega) = n(\omega)\omega/c$ becoming then a function of the frequency-dependent refractive index $n(\omega) = \sqrt{1 + \chi^{(1)}(\omega)}$. In that case, the UPPE code iterates the solution by always using equation (A.1) for solving the linear part and by performing the substitutions $\chi^{(3)} \to \chi^{(3)}/n(\omega_0)$ and $c\mu_0 \to c\mu_0/n(\omega)$ into the left-hand side and the right-hand side of equation (A.2) of the nonlinear contribution, respectively. In the MAXFLU1D code the only change consists in implementing the convolution product $\chi^{(1)} * E_x$ in the right-hand side of the equation (A.8).

ORCID iDs

J Déchard https://orcid.org/0000-0002-9767-7012
S Skupin https://orcid.org/0000-0002-9215-1150
L Bergé https://orcid.org/0000-0002-5531-7692

References

[1] Jackson J D 1975 *Classical Electrodynamics* (New York: Wiley)
[2] Kolesik M, Moloney J V and Mlejnek M 2002 Unidirectional optical pulse propagation equation *Phys. Rev. Lett.* **89** 283902
[3] Kolesik M and Moloney J V 2004 Nonlinear optical pulse propagation simulation: from Maxwell's to unidirectional equations *Phys. Rev.* E **70** 036604
[4] Andreasen J and Kolesik M 2012 Nonlinear propagation of light in structured media: generalized unidirectional pulse propagation equation *Phys. Rev.* E **86** 036706
[5] Köhler C, Cabrera-Granado E, Babushkin I, Bergé L, Herrmann J and Skupin S 2011 Directionality of terahertz emission from photoinduced gas plasmas *Opt. Lett.* **36** 3166
[6] Babushkin I, Skupin S, Husakou A, Köhler C, Cabrera-Granado E, Bergé L and Herrmann J 2011 Tailoring terahertz radiation by controlling tunnel photoionization events in gases *New J. Phys.* **13** 123029
[7] Kinsler P 2010 Optical pulse propagation with minimal approximations *Phys. Rev.* A **81** 013819
[8] Amiranashvili S and Demircan A 2010 Hamiltonian structure of propagation equations for ultrashort optical pulses *Phys. Rev.* A **82** 013812
[9] Babushkin I and Bergé L 2014 The fundamental solution of the unidirectional pulse propagation equation *J. Math. Phys.* **55** 032903
[10] Kim K Y, Taylor A J, Glownia J H and Rodriguez G 2008 Coherent control of terahertz supercontinuum generation in ultrafast laser-gas interactions *Nat. Photon.* **2** 605
[11] Bergé L, Skupin S, Köhler C, Babushkin I and Herrmann J 2013 3D numerical simulations of THz generation by two-color laser filaments *Phys. Rev. Lett.* **110** 073901
[12] González de Alaiza Martínez P, Davoine X, Debayle A, Gremillet L and Bergé L 2016 Terahertz radiation driven by two-color laser pulses at near-relativistic intensities: competition between photoionization and wakefield effects *Sci. Rep.* **6** 26743
[13] Thiele I, Nuter R, Bousquet B, Tikhonchuk V, Skupin S, Davoine X, Gremillet L and Bergé L 2016 Theory of terahertz emission from femtosecond-laser-induced microplasmas *Phys. Rev.* E **94** 063202
[14] Shkurinov A P, Sinko A S, Solyankin P M, Borodin A V, Esaulkov M N, Annenkov V V, Kotelnikov I A, Timofeev I V and Zhang X-C 2017 Impact of the dipole contribution on the terahertz emission of air-based plasma induced by tightly focused femtosecond laser pulses *Phys. Rev.* E **95** 043209
[15] Andreeva V A *et al* 2016 Ultrabroad terahertz spectrum generation from an air-based filament plasma *Phys. Rev. Lett.* **116** 063902
[16] Nodland B and McKinstrie C J 1997 Propagation of a short laser pulse in a plasma *Phys. Rev.* E **56** 7174
[17] Nicholson D R 1983 *Introduction to Plasma Theory* (New York: Wiley)
[18] Fibich G, Ilan B and Tsynkov S 2002 Computation of nonlinear backscattering using a high-order numerical method *J. Sci. Comput.* **17** 351
[19] Bergé L, Skupin S, Nuter R, Kasparian J and Wolf J P 2007 Optical ultrashort filaments in weakly-ionized, optically-transparent media *Rep. Prog. Phys.* **70** 1633
[20] Landau L D and Lifshitz E M 1965 *Quantum Mechanics* (New York: Pergamon)
[21] Thomson M D, Kress M, Löffler T and Roskos H G 2007 Broadband THz emission from gas plasmas induced by femtosecond optical pulses: from fundamentals to applications *Laser Photonics Rev.* **1** 349
[22] González de Alaiza Martínez P and Bergé L 2014 Influence of multiple ionization in laser filamentation *J. Phys. B: At. Mol. Opt. Phys.* **47** 204017
[23] Debayle A, Gremillet L, Bergé L and Köhler C 2014 Analytical model for THz emissions induced by laser–gas interaction *Opt. Express* **22** 13691
[24] Nguyen A, González de Alaiza Martínez P, Déchard J, Thiele I, Babushkin I, Skupin S and Bergé L 2017 Spectral dynamics of THz pulses generated by two-color laser filaments in air: the role of Kerr nonlinearities and pump wavelength *Opt. Express* **25** 4720

[25] Perelomov A M, Popov V S and Terent'ev M V 1966 Ionization of atoms in an alternating electric field *Sov. Phys. JETP* **23** 924
[26] Agrawal G P 2001 *Nonlinear Fiber Optics* 3rd edn (San Diego: Academic Press)
[27] LeVeque R J 2002 *Finite Volume Methods for Hyperbolic Equations* (New York, USA: Cambridge University Press)
[28] Toro E F 2012 *Riemann Solvers and Numerical Methods for Fluid Dynamics: A Practical Introduction* (Berlin: Springer)
[29] Anderson D and Lisak M 1983 Nonlinear asymmetric self-phase modulation and self-steepening of pulses in long optical waveguides *Phys. Rev.* A **27** 1393
[30] Lax P and Wendroff B 1960 Systems of conservation laws *Commun. Pure Appl. Math.* **13** 217
[31] Zalesak S T 2012 *Flux Corrected Transport: Principles, Algorithms, and Applications* (Berlin: Springer)